

AILERON EFFICIENCY ANALYSIS OF FLEXIBLE HIGH-ASPECT-RATIO WING

Yue Zhao[1,2], Jiawen He[1,2], Xinyuan Wei[1,2], Tieren Chen[1,2] & Yong Yang[1,2,*]

[1]School of Aeronautics, Northwestern Polytechnical University, Xi'an, 710072, PR China
[2]National Key Laboratory of Aircraft Configuration Design, Xi'an, 710072, PR China

Abstract

This paper investigates the aileron efficiency of the flexible high-aspect-ratio wing, which representing a prevailing design approach of high-altitude long-endurance aircraft and commercial airliners. To address the accurate impacts of aeroelastic deformations on static aileron efficiency and dynamic roll maneuverability, the simulation study leverages an aeroelastic-flight dynamics platform, which captures geometrically nonlinear effects induced by large deformations and analyzes aileron efficiency by deflecting ailerons at various spanwise locations. The key contributions of this paper are summarized as follows: First, an enhanced modal approach is developed on the basis of the traditional modal approach. This method retains the inherent simplicity of modal approach while capturing the geometric nonlinearities arising from large structural deformations. Second, the influence of aeroelastic deformations on the static aileron control efficiency of HARW is quantitatively studied. Third the influence of aeroelastic deformations on free-flight dynamic roll maneuverability is clarified for flexible HARW with the roll degree of freedom released.

Keywords: Aeroelasticity, High-aspect-ration wing, Aileron efficiency, Geometrically nonlinear

1. Introduction

In recent years, aircraft design has been moving towards the direction of increasing lift and reducing drag to achieve the goal of high efficiency and environmental friendliness. High-aspect-ratio wings (HARWs), due to their lower induced drag, have demonstrated superior aerodynamic characteristics and widely used in the design of high-altitude long-endurance (HALE) aircraft and civil airliners[1]. Nevertheless, HARWs have the characteristic of high flexibility. Affected by aerodynamic loads, the wings will undergo significant bending and torsional deformations, resulting in strong aero-structural coupling phenomena. In such situation, the impacts of aeroelasticity on aircraft aerodynamic characteristics and aileron efficiency have become increasingly important and non-negligible.

With the increase of aspect ratio and lightweight structural design, the flexibility of the wing rises significantly. Under aerodynamic loads, lightweight flexible high-aspect-ratio wings undergo large bending and torsional deformations. The stable state of the structure under loading exhibits obvious geometric differences from the original configuration, and the small deformation assumption adopted in the conventional linear analysis framework no longer applicable. Nevertheless, the internal strain of the wing structure remains small, and the stress–strain relationship of the material stays within the linear elastic range. Therefore, aeroelastic analysis of high-aspect-ratio wings must account for this effect of large displacement but small strain, which named geometric nonlinearity[3].

Compared with linear systems, geometric nonlinearity is mainly reflected in the following aspect:

High-aspect-ratio flexible wings exhibit obvious spanwise displacement under large deformation, which is defined as the shortening effect. If geometric nonlinearity is ignored, the projected area of the wing remains unchanged, but in fact the projected area changes significantly after deformation[4].

During flight, an aircraft controls its flight direction by deflecting control surfaces. As a primary mechanical component of the aircraft flight control system, control surface deflection generates variations in aerodynamic moments for the whole vehicle, and controls the aircraft's pitch, roll, yaw, as well as various maneuvering motions, thereby achieving precise flight attitude control. Therefore, determining the control efficiency of control surfaces is extremely crucial during the design phase of the aircraft control system module.

As one of the primary control surfaces of aircraft, ailerons are generally arranged at the outer part of

the wing. Differential deflection of ailerons produces rolling moments to drive the aircraft into rolling motion. Hence, research on aileron control efficiency and precise aileron control constitute an important research topic in the field of high-aspect-ratio wing studies. Furthermore, high-aspect-ratio aircraft are usually equipped with multiple aileron control surfaces, and aeroelastic effects impose influences of various degrees on the aileron control efficiency at different spanwise positions. Accordingly, it is very important to analyze the effects of aileron spanwise layout and aeroelasticity on aileron control efficiency.

To accurately obtain the structural deformation of high-aspect-ratio wings under aerodynamic loads, numerous scholars have carried out extensive exploratory research. In terms of wind tunnel experiments, Airbus collaborated with the University of Bristol in 2018 and conducted systematic wind tunnel tests on a high-aspect-ratio wing model in the 12ft×12ft low-speed wind tunnel at the Airbus Filton facility, based on the Agile Wing Integration (AWI) project. In terms of numerical computation, Ritter et al. proposed an enhanced modal method. By introducing high-order stiffness terms and high-order modal components, this method retains the simplicity of the traditional modal method while overcoming its inherent limitation in capturing geometric nonlinearity under large deformation. Taking the X-HALE UAV developed by the University of Michigan as the research object, they performed fluid–structure interaction analysis in MSC Nastran, where beam elements were adopted for the structural model and the unsteady Vortex Lattice Method was employed to compute aerodynamic forces[5]. Aiming at the failure of linear analysis caused by the large-deformation geometric nonlinear effect of high-aspect-ratio wings under aerodynamic loads, Yang Zhichun from Northwestern Polytechnical University proposed an aeroelastic analysis method based on the Nastran, and conducted investigations on quasi-linear modal and flutter characteristics. Numerical examples show that geometric nonlinearity leads to a remarkable reduction in wing torsional frequency, and the nonlinear flutter velocity is lower than the linear flutter velocity[6].

Regarding aileron efficiency studies, X. F. He et al. developed a flexible wing model with aileron freeplay, and investigated the effects of aileron freeplay nonlinearity on limit cycle oscillations (LCO) by combining ground vibration tests and low-speed wind tunnel tests. The results demonstrated that increasing aileron freeplay leads to a significant reduction in flutter divergence speed and an overall increase in oscillation amplitude, while the aileron spanwise position changes the critical coupling state[7]. For the control surface layout of aeroelastic wing boxes, Stanford proposed a control surface layout optimization technique integrating the concept of topology optimization, taking the Common Research Model wing box as the research object[8].

In preliminary aeroelastic analysis, modal approach is widely utilized owing to its capability to simplify structural simulation and thus saving the computation resources. However, traditional modal approach (MA) fails to account for geometrically nonlinear effects under large deformation. While the finite element method (FEM) enables accurate capture of geometric nonlinearities, but has the problem of excessive computational costs. To address the aforementioned issues, this paper aims to investigate the influence of aeroelastic deformation on static aileron control efficiency and free-flight dynamic roll maneuverability of HARWs based on an aeroelastic-flight dynamics platform embedded with enhanced modal approach (EMA) .

2. Technical Foundation

The aeroelastic-flight dynamics platform of numerical simulation is established through the coupling of Computational Fluid Dynamics (CFD), Computational Structural Dynamics (CSD), and Flight Dynamics (FD). Within this platform, the EMA is adopted to capture the accurate influence of aeroelastic deformations. Aerodynamic characteristics, load distributions, aileron effectiveness, rolling responses and geometrically nonlinear effects under large deformation of the HARW wings are investigated based on the platform. This paper focuses on the static aileron control efficiency and dynamic roll maneuverability with the roll degree of freedom (DOF) produced by deflecting aileron at various spanwise locations.

2.1 CFD Governing Equation

The three-dimensional arbitrary Lagrange-Euler Navier-Stokes equations can be written as:

$$\frac{\partial \mathbf{Q}}{\partial t}+\frac{\partial \mathbf{F}}{\partial x}+\frac{\partial \mathbf{G}}{\partial y}+\frac{\partial \mathbf{H}}{\partial z}=0 \tag{1}$$

In Eq.(1), $\mathbf{Q}=\left[\rho,\rho u,\rho v,\rho w,\rho E\right]^{T}$ is the vector of conservative variables, ρ is density, u,v and w

are the components of velocity, E is total energy of per unit mass. $\mathbf{F},\mathbf{G}$ and $\mathbf{H}$ are flux terms in three coordinate directions.

$$\begin{aligned}\mathbf{F}&=[\rho u,\rho u^2+p-\tau_{xx},\rho uv-\tau_{xy},\rho uw-\tau_{xz},\rho Hu-b_x]\\ \mathbf{G}&=[\rho v,\rho uv-\tau_{yx},\rho v^2+p-\tau_{yy},\rho vw-\tau_{yz},\rho Hv-b_y]\\ \mathbf{H}&=[\rho w,\rho uw-\tau_{zx},\rho vw-\tau_{zy},\rho w^2+p-\tau_{zz},\rho Hw-b_z]\end{aligned} \tag{2}$$

In Eq. (2), p is pressure, H is total enthalpy of per unit mass, τ_{ij} is viscous shear stress.

2.2 EMA Governing Equation

The modal approach reduces the order of the physical displacement expansion via modal truncation, which lowers the computational cost of the structural governing equations. When structural damping is ignored, the corresponding modal equation is given as follows.

$$\{u\}=[\phi]\{q\}=\sum_{i=1}^{n}q_i(t)\{\phi\}_i \tag{3}$$

Where $q_i(i=1,2,\cdots,n)$ denotes the modal displacement of each order, $\{\phi\}_i=[\phi_1^{(i)}\quad\phi_2^{(i)}\quad\cdots\quad\phi_m^{(i)}]^T$ is the corresponding mode shape, and $\{u\}$ represents the physical displacement vector in the structural coordinate system. But this method is only applicable to linear deformation. Therefore, to retain the simplicity of the modal method while capturing the geometric nonlinear effect induced by large structural deformations, this paper improves the traditional modal approach. By introducing high-order modal components and high-order stiffness terms, the EMA captures the geometric nonlinearity arising from large structural deformations[9].

From the conservation of total potential energy:

$$\pi=U+V=const \tag{4}$$

where U represents the structural strain energy, and V is the external load potential energy.

Expressing the external load potential energy in the form of the product of nodal forces and nodal displacements:

$$\pi=U+V=U-\sum_{i=1}^{m}P_i\Delta_i=const \tag{5}$$

Taking the partial derivative of the nodal displacement with respect to the i-th node yields:

$$\frac{\partial U}{\partial \Delta_i}=P_i \tag{6}$$

Extended to modal coordinates:

$$\frac{\partial U}{\partial q_i}=Q_i \tag{7}$$

The physical meaning of Eq. (7) is that the partial derivative of the strain energy with respect to a certain modal displacement equals the generalized force in the corresponding direction. Regarding the strain energy as a function of modal displacement $\boldsymbol{q}=(q_1,\cdots,q_m)^T$, the strain energy U is expanded by the Taylor series at $\boldsymbol{q}$=0:

$$U(\boldsymbol{q})=\frac{1}{2!}\sum_{i=1}^{m}\sum_{j=1}^{m}\frac{\partial^2U}{\partial q_i\partial q_j}q_iq_j+\frac{1}{3!}\sum_{i=1}^{m}\sum_{j=1}^{m}\sum_{k=1}^{m}\frac{\partial^3U}{\partial q_i\partial q_j\partial q_k}q_iq_jq_k+h.o.t \tag{8}$$

Since the constant term and linear term contribute nothing to the strain energy, they can be omitted in the Taylor expansion. Taking the partial derivative with respect to the modal displacement in the $q_p(p=1,\cdots,m)$ direction yields:

$$\frac{\partial U(\boldsymbol{q})}{\partial q_p}=\sum_{i=1}^{m}\frac{\partial^2U}{\partial q_i\partial q_p}q_i+\frac{1}{2!}\sum_{i=1}^{m}\sum_{j=1}^{m}\frac{\partial^3U}{\partial q_i\partial q_j\partial q_p}q_iq_j+\frac{1}{3!}\sum_{i=1}^{m}\sum_{j=1}^{m}\sum_{k=1}^{m}\frac{\partial^4U}{\partial q_i\partial q_j\partial q_k\partial q_p}q_iq_jq_k+h.o.t=Q^P \tag{9}$$

where Q^P denotes the generalized force corresponding to the q_p direction, and each coefficient

constitutes the corresponding stiffness coefficient matrix. The quadratic stiffness, cubic stiffness and quartic stiffness are expressed respectively as:

$$ {}^{p}G_1^i = \sum_{i=1}^{m} \frac{\partial^2 U}{\partial q_i \partial q_p} \tag{10} $$

$$ {}^{p}G_2^{ij} = \frac{1}{2!} \sum_{i=1}^{m} \sum_{j=1}^{m} \frac{\partial^3 U}{\partial q_i \partial q_j \partial q_p} \tag{11} $$

$$ {}^{p}G_3^{ijk} = \frac{1}{3!} \sum_{i=1}^{m} \sum_{j=1}^{m} \sum_{k=1}^{m} \frac{\partial^4 U}{\partial q_i \partial q_j \partial q_k \partial q_p} \tag{12} $$

Similarly, the nodal displacement u is expanded in a Taylor series at $\boldsymbol{q}$=0:

$$ u(\boldsymbol{q}) = \sum_{i=1}^{m} \frac{\partial u}{\partial q_i} q_i + \frac{1}{2!} \sum_{i=1}^{m} \sum_{j=1}^{m} \frac{\partial^2 u}{\partial q_i \partial q_j} q_i q_j + \frac{1}{3!} \sum_{i=1}^{m} \sum_{j=1}^{m} \sum_{k=1}^{m} \frac{\partial^3 u}{\partial q_i \partial q_j \partial q_k} q_i q_j q_k + h.o.t \tag{13} $$

Since the nodal displacement is zero at $\boldsymbol{q}$=0, the constant term can be omitted. Taking the partial derivative with respect to the modal displacement in the $q_p\,(p = 1, \cdots, m)$ direction yields:

$$ \frac{\partial u(\boldsymbol{q})}{\partial q_p} = \frac{\partial u}{\partial q_p} + \sum_{i=1}^{m} \frac{\partial^2 u}{\partial q_i \partial q_p} q_i + \frac{1}{2!} \sum_{i=1}^{m} \sum_{j=1}^{m} \frac{\partial^3 u}{\partial q_i \partial q_j \partial q_p} q_i q_j + h.o.t = {}^{p}\Phi \tag{14} $$

The linear, quadratic, and cubic modal components are extracted separately:

$$ {}^{p}\Phi_0 = \frac{\partial u}{\partial q_p} \tag{15} $$

$$ {}^{p}\Phi_1^i = \sum_{i=1}^{m} \frac{\partial^2 u}{\partial q_i \partial q_p} \tag{16} $$

$$ {}^{p}\Phi_2^{ij} = \frac{1}{2!} \sum_{i=1}^{m} \sum_{j=1}^{m} \frac{\partial^3 u}{\partial q_i \partial q_j \partial q_p} \tag{17} $$

When the structure is subjected to the external load $\boldsymbol{f}$:

$$ \delta u = \delta q_p \left({}^{p}\Phi_0 + {}^{p}\Phi_1^i q_i \right) \tag{18} $$

According to the principle of virtual work:

$$ \delta V = \delta u^T \boldsymbol{f} \tag{19} $$

The nodal displacement is represented by the first two terms in Eq. (14):

$$ \delta u = \delta q_p \left({}^{p}\Phi_0 + {}^{p}\Phi_1^i q_i \right) \tag{20} $$

$$ \delta V = \delta q_p^T \left({}^{p}\Phi_0^T + {}^{p}\Phi_1^{iT} q_i \right) \boldsymbol{f} \tag{21} $$

Thus, the generalized force can be obtained. Substituting it into Eq. (9):

$$ \left({}^{p}G_1^i - {}^{p}\Phi_1^{iT} \boldsymbol{f} \right) q_i + {}^{p}G_2^{ij} q_i q_j + {}^{p}G_3^{ijk} q_i q_j q_k = {}^{p}\Phi_0^T \boldsymbol{f} \tag{22} $$

The discrete n-th EMA equation can been written as:

$$ u(\boldsymbol{q}) = {}^{p}\Phi_0 q_p + {}^{p}\Phi_1^i q_p q_i + {}^{p}\Phi_2^{ij} q_p q_i q_j + {}^{p}\Phi_3^{ijk} q_p q_i q_j q_k \tag{23} $$

In Eq.(23), $\{u(\boldsymbol{q})\}$ is physical displacement vector of nodes, q_p is p-th order modal displacement of nodes, Φ_m is m-th modal shape of nodes which obtained by numerical difference operation such as:

$$ {}^{1}\Phi_1^1 = \frac{\partial^2 u}{\partial^2 q_1} \approx \frac{u(\Delta q_1) - 2u(0) + u(-\Delta q_1)}{\Delta {q_1}^2} \tag{24} $$

In Eq. (24), $u(\Delta q_1)$ and $u(-\Delta q_1)$ are displacements obtained from two opposite force loads applied on the nodes in the first order modal shape. This process is implemented by ANSYS Modal with FEM.

$$ F_1 = [\boldsymbol{K}] u(\Delta q_1) \tag{25} $$

In Eq. (25), F_1 is the force load on nodes, $[\boldsymbol{K}]$ is stiffness matrix.

In the EMA coupled with the computational platform in this paper, only first two terms of Equation (23) are employed to capture geometrically nonlinear effects under large deformation, while the higher-order terms are neglected.

2.3 FD Governing Equation

The Quasi-Coordinate flexible aircraft flight dynamic equation based on the Lagrange equation can been written as[10]:

$$\begin{aligned} &\frac{d}{dt}\left(\frac{\partial L}{\partial \boldsymbol{V}}\right)+\tilde{\boldsymbol{\omega}}\frac{\partial L}{\partial \boldsymbol{V}}-C\frac{\partial L}{\partial \boldsymbol{R}}=\boldsymbol{F} \\ &\frac{d}{dt}\left(\frac{\partial L}{\partial \boldsymbol{\omega}}\right)+\tilde{\boldsymbol{V}}\frac{\partial L}{\partial \boldsymbol{V}}+\tilde{\boldsymbol{\omega}}\frac{\partial L}{\partial \boldsymbol{\omega}}-(\boldsymbol{E}^{T})^{-1}\frac{\partial L}{\partial \boldsymbol{\theta}}=\boldsymbol{M} \\ &\frac{\partial}{\partial t}\left(\frac{\partial \hat{T}}{\partial \tilde{\boldsymbol{v}}}\right)-\frac{\partial \hat{T}}{\partial \tilde{\boldsymbol{u}}}+\frac{\partial \tilde{\mathcal{F}}}{\partial \tilde{\boldsymbol{v}}}+\mathcal{L}\tilde{\boldsymbol{u}}=\hat{\boldsymbol{U}} \end{aligned} \tag{26}$$

In equation (26), L is the difference between total kinetic energy and total potential energy of the system; $\boldsymbol{R}$ is radius vector of aircraft centroid; C is transformation matrix from inertial coordinate system to aircraft body coordinate system; $\boldsymbol{V}$, $\boldsymbol{\omega}$ is the velocity, angular velocity of aircraft in quasi-coordinate, $\tilde{\boldsymbol{V}}$, $\tilde{\boldsymbol{\omega}}$ is antisymmetric tensor of $\boldsymbol{V}$, $\boldsymbol{\omega}$; $\tilde{\boldsymbol{u}}, \tilde{\boldsymbol{v}}$ is the deformation and the corresponding time derivative of aircraft in quasi-coordinate; $\boldsymbol{\theta}$, $\boldsymbol{E}$ is Euler angle and transformation matrix from inertial coordinate to quasi-coordinate; $\hat{T}$ is density function of aircraft; $\tilde{\mathcal{F}}$ is Rayleigh dissipation matrix; $\mathcal{L}$ is stiffness matrix differential operator; $\boldsymbol{F}$, $\boldsymbol{M}$, $\hat{\boldsymbol{U}}$ are generalized force.

Consider the elastic aircraft shown in Figure 1. B_0 represents the initial configuration, and B_d denotes the deformed configuration. The inertial coordinate system $O_G X_G Y_G Z_G$ is fixed to the ground, while the origin of the body coordinate system $O_b x_b y_b z_b$ is located at the mass center of the aircraft.

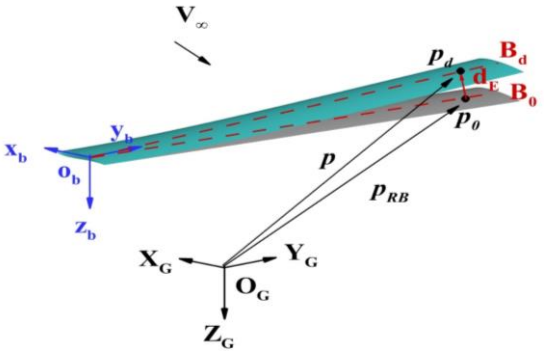


Figure 1 Elastic Aircraft

The position of an arbitrary point $\boldsymbol{p}$ on the aircraft can be expressed as the sum of its position $\boldsymbol{p}_{RB}$ relative to the mass center in the rigid-body state and its elastic deformation $\boldsymbol{d}_E(x,y,z,t)$, as shown in Eq.(27):

$$\boldsymbol{p}=\boldsymbol{p}_{RB}+\boldsymbol{d}_E(x,y,z,t) \tag{27}$$

Under the assumption of linear elasticity, the elastic deformation $\boldsymbol{d}_E(x,y,z,t)$ can be decomposed into a linear combination of mode shapes and modal coordinates:

$$\boldsymbol{d}_E(x,y,z,t)=\sum_{i=1}^{n}\phi_i(x,y,z)q_i(t) \tag{28}$$

Schmidt et al. adopted the concept of mean axes and demonstrated the existence of a special body coordinate system[11]. In this coordinate system, the linear momentum and angular momentum generated by the unforced oscillation of the aircraft due to elastic deformation are identically 0, which simplifies the expressions of the total angular momentum and total kinetic energy:

$$\iiint_V \frac{d\boldsymbol{d}_E}{dt}\hat{\rho}dV = \iiint_V \boldsymbol{p}_{RB} \times \frac{d\boldsymbol{d}_E}{dt}\hat{\rho}dV = 0 \tag{29}$$

Where $\hat{\rho}$ denotes the density distribution function of the aircraft. Equation (29) is also known as the mean axis constraint. In most cases, the mean axes of the aircraft coincide with its principal axes. Under the small deformation assumption, the moments of inertia are still assumed to be constant. The mean axes are selected as the body coordinate system fixed to the aircraft for the derivation of the six-degree-of-freedom aircraft dynamic equations. Under the mean axis assumption, the governing equations for elastic deformation and rigid degrees of freedom can be decoupled. The elastic deformation motion and rigid body motion interact with each other through aerodynamic loads.

2.4 CFD/CSD/FD Coupling Method

This paper simulates the response of flexible aircraft based on CFD/CSD/FD loose coupling method with estimation correction step, as shown in Figure 2.

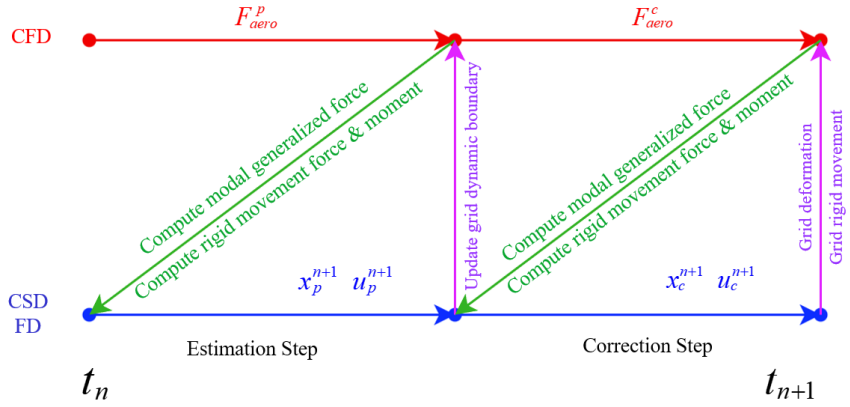


Figure 2 Coupling computing process

2.5 EMA Numerical Verification

To verify the accuracy of the EMA in capturing the geometric nonlinear effects of flexible wings under large deformation, a straight HALE wing as the numerical example in this section. Coupled calculations are carried out based on the MA and EMA with CFL3D as the flow solver, as well as coupled computations based on the FEM with ANSYS FLUENT. The static aeroelastic deformation results and lift coefficients of the wing are obtained and compared with the numerical results published by Smith M J et al. The geometric model and structural parameters of the wing are presented as follows[12].

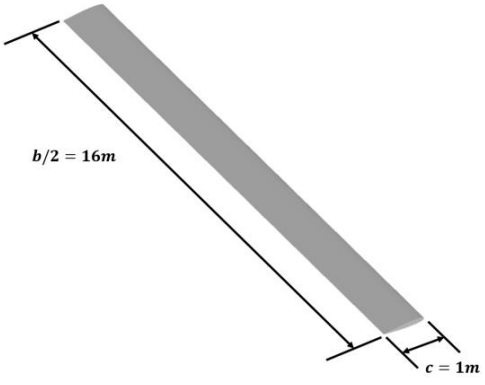


Figure 3 HALE Wing

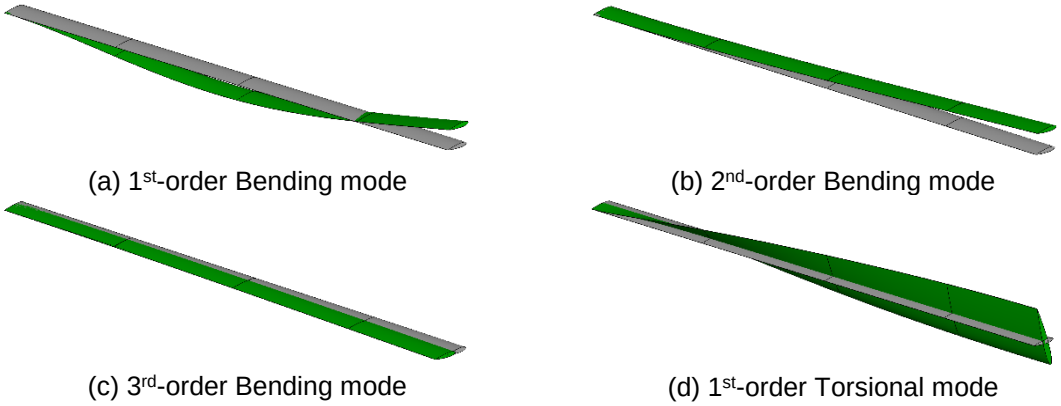
Table 1 Geometry and Structure Parameters

Semi-Span	16.0 m
Chord Length	1.0 m
Mass	12 kg
Density	9.125 kg/m^3
Area product of inertia	6.7877×10^{-5}m^4
Polar moment of inertia	7.632×10^{-5}m^4
Bending Stiffness	5×10^{6}N • m
Young's modulus	0.29465Gpa
Shear modulus	0.14733Gpa
Poisson's ratio	0.31

Structural modal analysis is performed on the HALE wing, and the four modal frequencies are compared with the reference results and listed in Table 2. The corresponding mode shapes are shown in Figure 3, where the gray surface represents the original configuration of the wing, and the green surface denotes each order of modal shape.

Table 2 Modal Analysis Results

Mode	Present(rad/s)	Reference(rad/s)	Error(%)
1st-order Bending mode	2.259	2.243	0.71
2nd-order Bending mode	14.128	14.056	0.51
3rd-order Bending mode	18.063	18.028	0.19
1st-order Torsional mode	31.377	31.046	1.06



(a) 1st-order Bending mode (b) 2nd-order Bending mode

(c) 3rd-order Bending mode (d) 1st-order Torsional mode

Figure 4 Modal Shape

The modes in Figure 4 are interpolated onto the aerodynamic grid for linear aeroelastic calculations. For nonlinear calculations, two opposite force loads are applied on the nodes of the 1st-order Bending mode. The FEM is employed to get two physical displacements, which are differenced to obtain higher-order modes according to Equation(24). These higher-order modes are interpolated onto the aerodynamic grid to solve nonlinear static aeroelastic deformations.

The calculation conditions are consistent with those in the references: altitude of 20 km, flight speed of 25 m/s, angle of attack of 4°. The Z-coordinates of the leading-edge point of the deformed wing calculated by different methods are compared with the reference results in Figures 4 and 5. Herein, Ref_linear and Ref_nonlinear denote the results obtained by the linear and nonlinear algorithms in the references[12],[13].

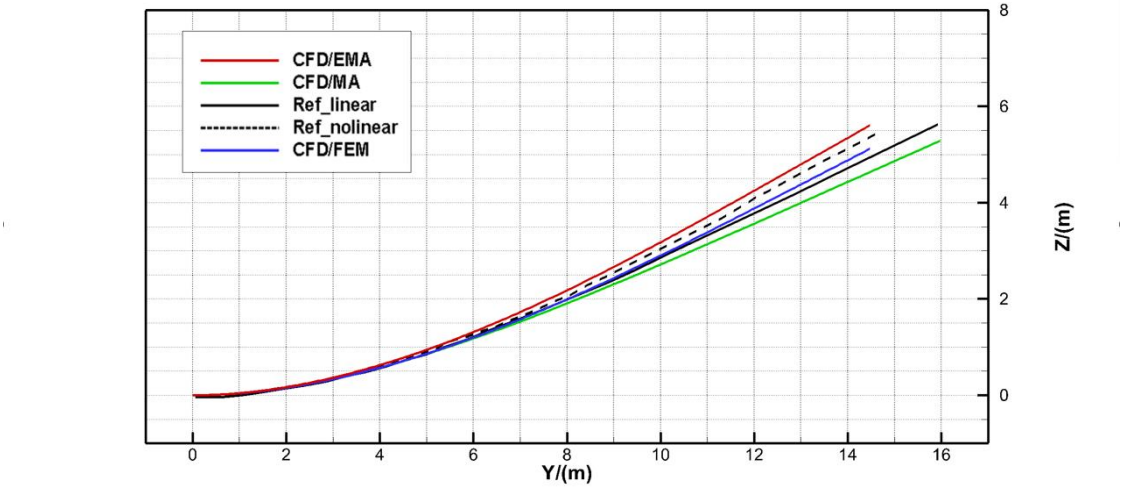


Figure 5 HALE Wing Aeroelastic Deformation at =4°

The lift and drag coefficients, lift-to-drag ratio(L/D), as well as the wingtip deformations along the Y-axis and Z-axis obtained by the MA-based, EMA-based and FEM-based coupled methods adopted in this paper are compared in Table 3.

Table 3 Comparison of Aerodynamic Characteristic and Deformation

Parameter	CFD/MA	CFD/EMA	CFD/FEM
CL	0.5265	0.4794	0.4656
Vertical Deformation (m)	5.27	5.60	5.11
Horizontal Deformation (m)	0.00	1.50	1.51
CPU time	16cores ×17h	16cores×17h	16cores×314h

It can be seen from the comparison of the static aeroelastic deformation results of the HALE wing that the CFD/CSD coupled method based on the EMA can well capture the geometric nonlinear phenomena of the wing under large deformation, and has a good agreement with the results given in the references. From the comparison of various coupling methods in Figure 5, the result based on the EMA shows geometrically nonlinear effects induced by large deformation geometrically.

From the comparison of the lift coefficient, wingtip deformation and computational core time consumption obtained by the three methods in Table 3, it is found that when the traditional linear MA is used for aeroelastic calculation, the lift is larger due to the failure to capture the shortening of the spanwise deformation. In contrast, the FEM can capture the geometric nonlinearity of the wing under large deformation, but it consumes excessive core time. However, the EMA not only can well capture the geometric nonlinearity, but also requires computational resources similar to those of the traditional modal approach. This indicates that the EMA can accurately capture the geometric nonlinear effects of the wing under large flexible deformation while maintaining the simplicity in solving structural deformation.

3. Static Aileron Effectiveness Analysis of CRM Wing

During flight, high-aspect-ratio flexible wings undergo non-negligible aeroelastic deformation under aerodynamic loads. As a primary control surface for regulating the lateral motion of aircraft, the aileron frequently suffers from reduced control efficiency and even control reversal under the influence of aeroelastic deformation. Considering the geometric nonlinear effects induced by large flexible deformation, this chapter takes the wing configuration of the Common Research Model (CRM) transport aircraft as the research object and selects its right wing as the computational model. The TFI mesh deformation technique is adopted to simulate real aileron deflection. Loosely coupled CFD/CSD computations are carried out respectively based on the enhanced modal method and the linear modal method to analyze the effects of aeroelastic deformation and geometric nonlinearity on the aerodynamic characteristics and aileron control efficiency of the CRM wing. On this basis, the spanwise position of the aileron is adjusted to further explore the influences of aeroelastic deformation on aileron effectiveness at different spanwise locations.

3.1 Static Aeroelastic Analys

The aspect ratio of the CRM wing is 9.0. In this section, the wing span is stretched by a factor of 1.5 along the spanwise direction to increase the wing aspect ratio. The geometric configurations of the original and stretched CRM wings, and the structural parameters adopted in this paper are presented in Figure 6 and Table 4.

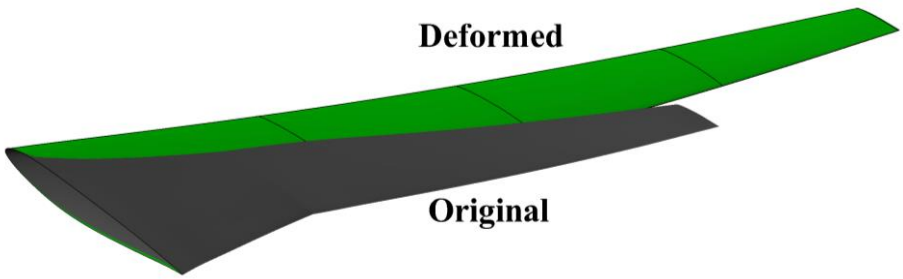


Figure 6 CRM Geometry

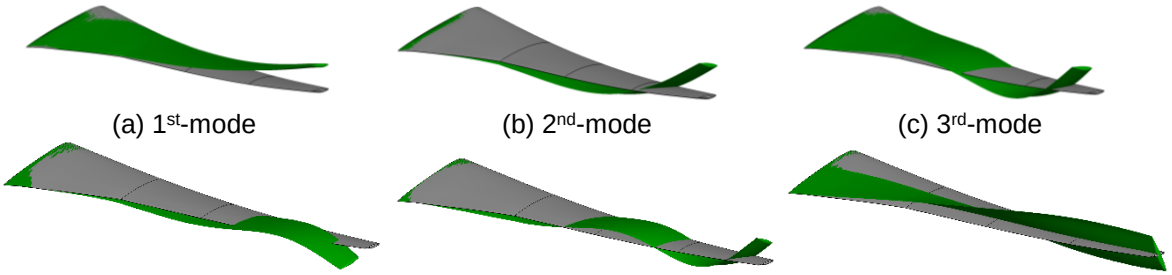
Table 4 Geometry and Structure Parameter

Parameter	Original	Deformed
Reference Area	111.09 m^2	249.95 m^2
Reference Chord	6.33 m	6.33 m
Semi - Span	26.37m	39.486 m
Taper Ratio	0.275	0.275
Aspect Ratio	9.0	13.5
Young's modulus (isotropic)	-	1.382Gpa
Shear modulus (isotropic)	-	1.954Gpa
Poisson's ratio	-	0.33

The model is defined as a homogeneous solid structure. Modal analysis is conducted for the CRM wing models with aspect ratios of 13.5. The comparison of modal frequencies is listed in Table 5, and the corresponding mode shapes are presented in Figure 7. The gray surface represents the original geometric shape of the wing, while the green surface denotes the mode shape of each order.

Table 5 Modal Frequency

mode	calculation(rad/s)
1st-mode	5.9973
2nd-mode	19.591
3rd-mode	42.229
4th-mode	49.620
5th-mode	75.877
6th-mode	106.20

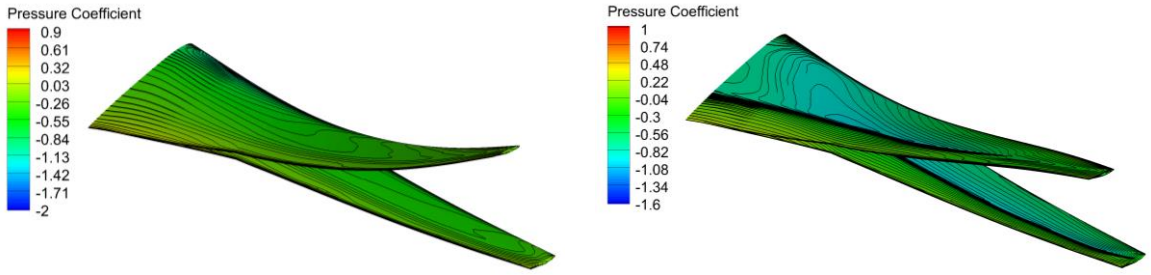


(a) 1st-mode (b) 2nd-mode (c) 3rd-mode

(d) 4th-mode (e) 5th-mode (f) 6th-mode

Figure 7 Modal Shape

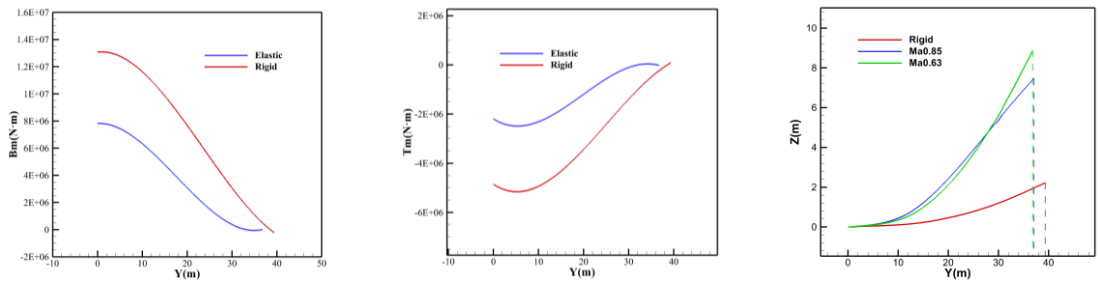
The modal analysis results are interpolated into the CFD computational grid. The static aeroelastic deformation of the CRM wing is numerically simulated using the EMA based CFD/CSD coupled method. The computational conditions are set at an altitude of 10 km, Mach numbers of 0.63 and 0.85, and angle of attack of 2°. The comparison of surface pressure contours between the rigid and elastic wings is presented as Figure 8.



(a) Ma=0.63 (b) Ma=0.85

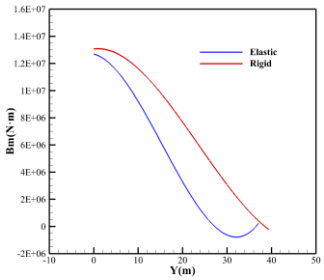
Figure 8 Static Aeroelastic Deformation

The spanwise distributions of leading-edge coordinates, section twist angles, bending moments, and torsional moments of the CRM wing before and after static aeroelastic deformation are extracted and presented in Figure 9 and Figure 10, while the variations in aerodynamic parameters are listed in Table 6.

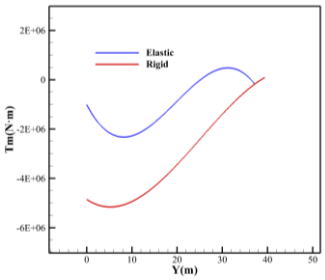


(a) Ma=0.63 Bending Moment (c) Ma=0.63 Torque (e) Vertical Deformation

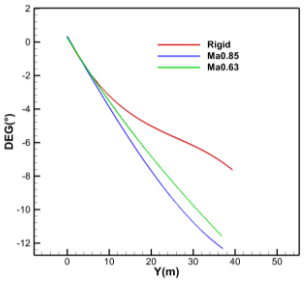
Figure 9 Ma=0.63 Aeroelastic Result



(b) Ma=0.85 Bending Moment



(d) Ma=0.85 Torque



(f) Torsion Angle

Figure 10 Aeroelastic Result

Table 6 Aerodynamic Parameters

	Rigid		Elastic	
	Mach=0.63	Mach=0.85	Mach=0.63	Mach=0.85
C_L	0.4671	0.5656	0.3521	0.3591
C_D	0.1271E-1	0.3239E-1	0.1206E-1	0.2356E-1
$C_{L/D}$	36.75	17.46	29.20	15.24

From the comparisons of aerodynamic coefficients in Table 6 and the sectional load distributions in Figure 9 and Figure 10, aeroelastic deformation alleviates wing-root bending moment, and torsional moment acting on the CRM wing. On the one hand, the deformation of the wing along the positive Z-axis reduces the local angle of attack of the wing section. On the other hand, aeroelastic deformation induces negative twist of the CRM wing, which further decreases the aerodynamic force and moment loads on the wing. The reduction in wing loads leads to a decrease in lift. Meanwhile, the lift-to-drag ratio of the deformed wing is obviously lower than that of the rigid configuration, resulting in a significantly deterioration of the aerodynamic efficiency.

Furthermore, by comparing the influence of aeroelastic effects on the wing at different Mach numbers, it is found that the wing deformation is dominated by the first-order bending mode at Ma 0.63, while a reverse bending phenomenon occurs at the wingtip when Ma 0.85. Comparing the bending moment distributions at different Mach numbers, the bending moment is positive across the total wing at Ma 0.63, whereas negative bending moment appears at the wingtip region at Ma 0.85. As for the twist angle distributions, the growth trend of wingtip torsion at Ma 0.85 is similar to that at Ma 0.63, with a slightly larger negative twist at the wingtip.

It can be concluded from the above results and analysis that structural deformation is coupled with the redistribution of aerodynamic loads for the CRM wing when aeroelasticity is considered. The geometric characteristics, twist and swept configuration of the CRM wing induce a more complex bending-torsion coupling effect under aeroelastic deformation. The numerical results indicate the aerodynamic loads and the aerodynamic efficiency of the wing have been reduced. This demonstrates the importance of taking aeroelastic effects into account in the aerodynamic characteristic analysis of high-aspect-ratio transonic aircraft.

3.2 Static Aileron Effectiveness Calculation with Aeroelasticity

For an aircraft, deflection of the ailerons is supposed to produce rolling motion about the aircraft longitudinal axis. But the aeroelastic effects of flexible wings degrade aileron control efficiency and may even lead to aileron reversal.

For the CRM wing, static aeroelastic deformation cause the remarkable impact on aerodynamic forces. Affected by aeroelastic deformation, the control efficiency of the aileron, as a typical wing control surface, is also significantly influenced. In this section, the TFI mesh deformation technique is employed to deform the local mesh of the aileron and simulate actual aileron deflection. On this basis, CFD/CSD coupled simulations are carried out to investigate the influence of aeroelastic deformation on static aileron effectiveness which also takes the semi-wing as the research object.

The ailerons are designed to occupy approximately 10% of the span and 25% of the local chord length in the chordwise direction. The hinge axis is arranged at the leading edge of the control surface, and the position and deflection of aileron are shown Figure 11 and Figure 12.

In the Figure 11 and Figure 12, AIL1-6 define various spanwise ailerons. The aileron is deflected downward by 5° and 10° . The calculation conditions are set at an altitude of 10 km with Mach numbers of 0.63 and 0.85. The structural parameters of the wing remain consistent with those given in the previous context. Adopting the CFD/CSD coupling method based on the EMA, the aileron effectiveness is obtained and presented in the Figure 13. The comparison of surface pressure contours between the rigid and elastic wings is presented as Figure 14 and Figure 15.

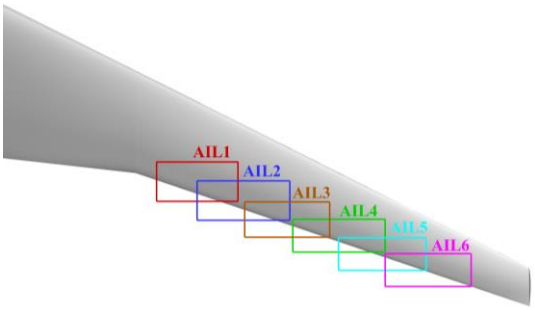


Figure 11 Ailerons Position

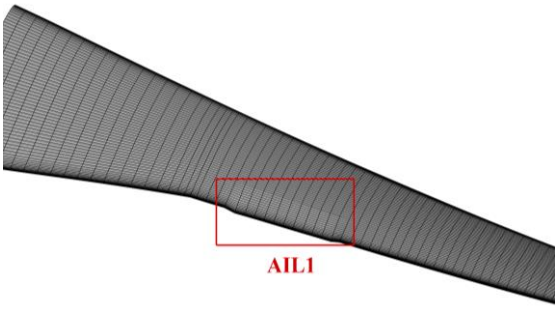
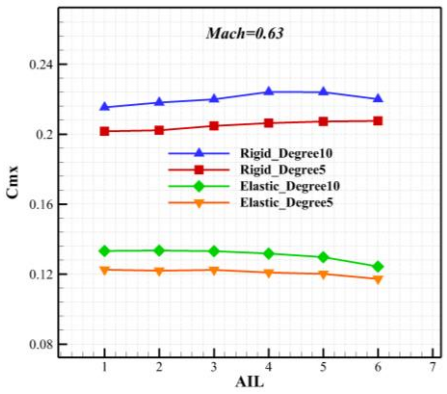
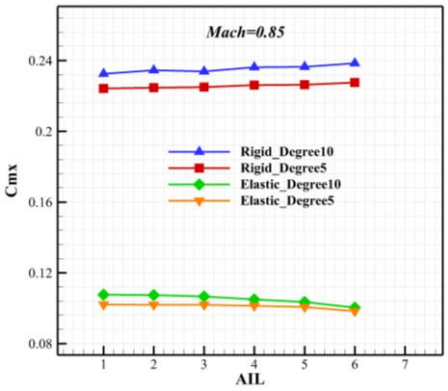


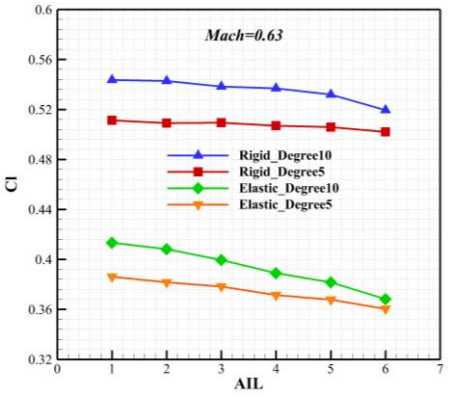
Figure 12 AIL1 Deflection 5°



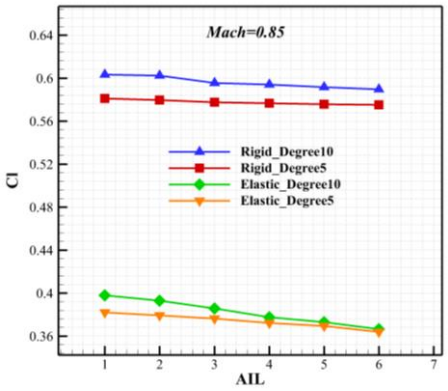
(a) Mach=0.63 AIL-Cmx



(b) Mach=0.85 AIL-Cmx

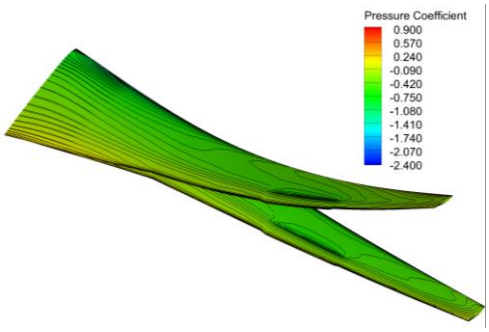


(c) Mach=0.63 AIL-Cl

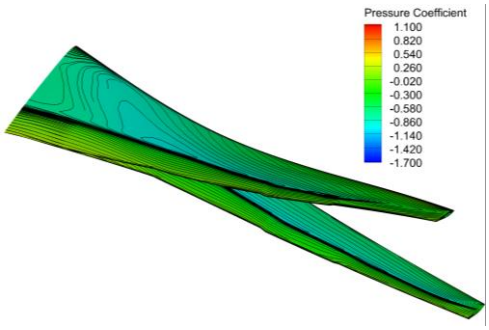


(d) Mach=0.85 AIL-CL

Figure 13 Aeroelasticity with Aileron Deflection

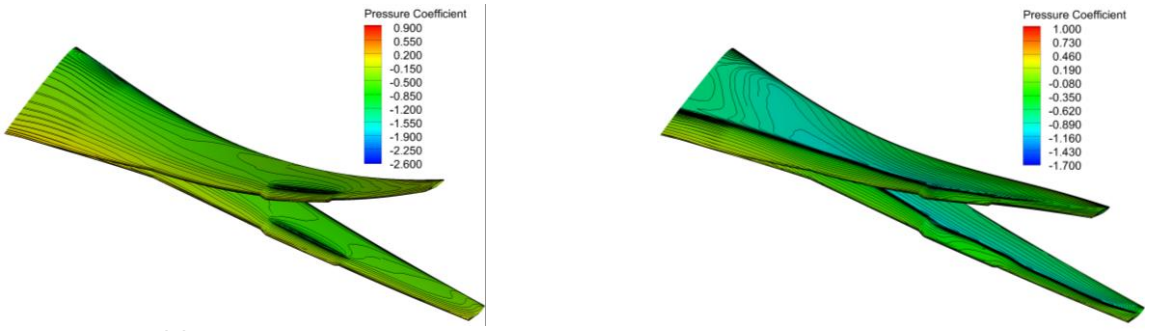


(a) Degree_5°



(b) Degree_10°

Figure 14 AIL4 Mach=0.63



(a) Degree_5° (b) Degree_10°

Figure 15 AIL4 Mach=0.85

It can be seen from Figure 13 that both the lift coefficient and rolling moment coefficient of the wing decrease significantly after aeroelastic deformation, with a corresponding decline in static aileron effectiveness. For the rigid wing, the rolling moment generated by aileron deflection increases as the aileron spanwise position moves outboard. The aileron effectiveness exhibits a trend of first increasing and then decreasing and reaching maximum at AIL4.In contrast, the elastic wing exhibits an opposite trend. Under the conditions of Mach 0.63 and 0.85, the roll moment coefficient and aileron effectiveness decrease as the aileron is arranged further outboard, and the lift coefficient follows the same variation tendency. At Mach 0.85, the roll moment coefficient induced by aileron deflection is lower than that at Mach 0.63, and the effectiveness of the outboard ailerons (AIL5, AIL6) is negligible, indicating that the Mach 0.85 flight condition is approaching the critical aileron reversal speed.

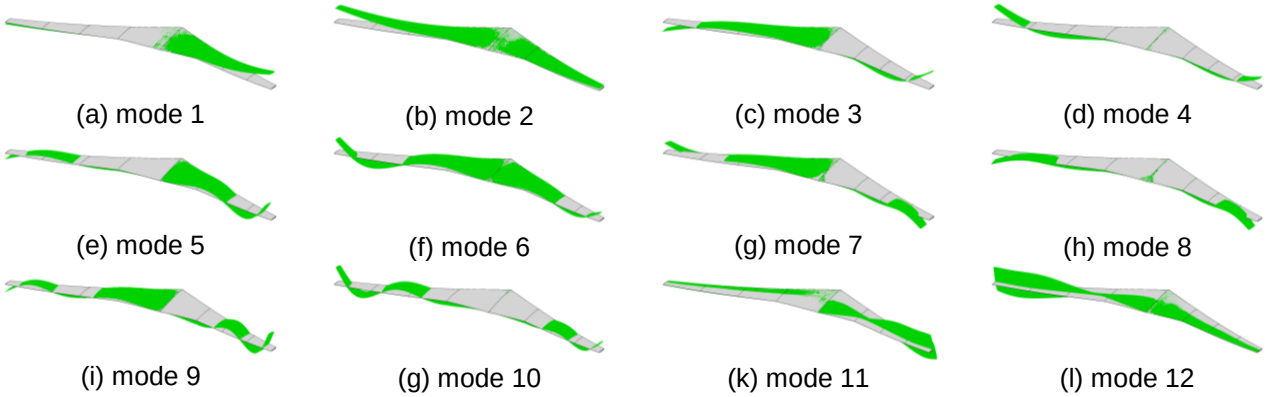
Based on the above numerical results and analysis, the impact of aeroelastic deformation on aileron effectiveness is non-negligible. Therefore, it is essential to take into account the aeroelastic effects when evaluating the static aileron control efficiency of high-aspect-ratio aircraft.

4. Dynamic Roll Maneuverability Analysis of CRM Wing

In actual flight, aircrafts perform rolling maneuvers by deflecting aileron differentially, hence the full span model should be considered. The TFI mesh deformation technique is employed to simulate aileron deflection, and static aeroelastic numerical simulations are conducted based on the EMA. Based on this, the roll degree of freedom is released to calculate the roll response of the full-model configuration after aileron deflection, which investigate the influence of aeroelastic deformation on the dynamic effectiveness of aileron and rolling maneuverability of the CRM configuration.

4.1 Static Aeroelastic Analys

A fixed support constraint is applied at the symmetry plane of the CRM full-model configuration. The material parameters are identical to those presented in Section 3.1. The results of the modal analysis are presented as Figure 16 and Table 7:



(a) mode 1 (b) mode 2 (c) mode 3 (d) mode 4

(e) mode 5 (f) mode 6 (g) mode 7 (h) mode 8

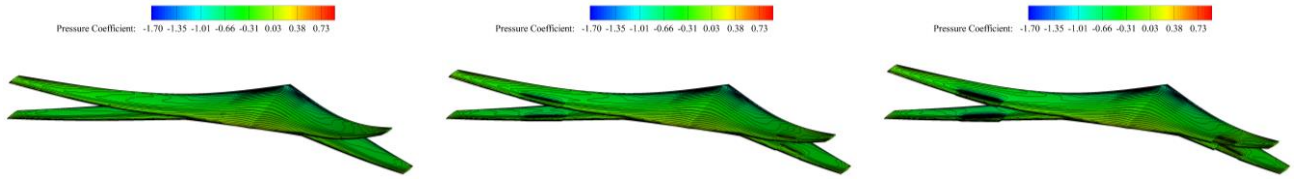
(i) mode 9 (g) mode 10 (k) mode 11 (l) mode 12

Figure 16 Modal Shape

Table 7 Modal Frequency

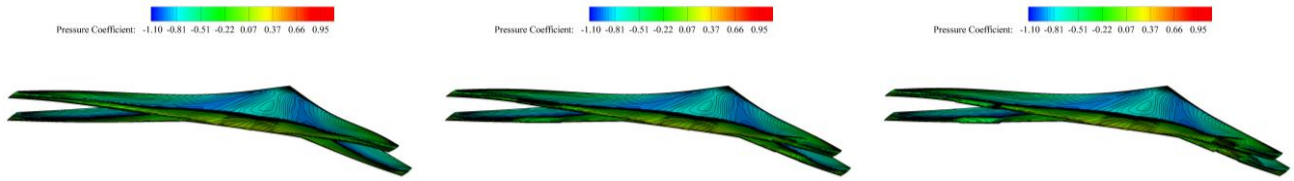
mode	calculation(rad/s)	mode	calculation(rad/s)
mode 1	6.0798	mode 7	49.6070
mode 2	6.0855	mode 8	49.6617
mode 3	19.9479	mode 9	77.6099
mode 4	19.9604	mode 10	77.7356
mode 5	42.9625	mode 11	109.3777
mode 6	43.0222	mode 12	109.5034

This section selects the AIL4, which exhibits medium effectiveness from Section 3.2, as the differentially deflected aileron with deflection angles of 5° and 10°. The pressure contours obtained from the static aeroelastic numerical simulations at Mach=0.63 and 0.85 are presented as Figure 17 and Figure 18. Comparisons of aerodynamic parameters under different aileron deflection angles between the aeroelastic and rigid configurations are presented in Table 8 and Table 9.



(a) 0° Deflection (b) 5° Deflection (c) 10° Deflection

Figure 17 Mach=0.63



(a) 0° Deflection (b) 5° Deflection (c) 10° Deflection

Figure 18 Mach=0.85

Table 8 Mach=0.63 Aerodynamic Parameters

	Rigid			Elastic		
Deflection	0°	5°	10°	0°	5°	10°
C_{mx}	0.5336E-6	0.1137E-1	0.2208E-1	0.1793E-4	0.6080E-2	0.1216E-1
C_L	0.4735E0	0.4727E0	0.4686E0	0.3501E0	0.3493E0	0.3474E0
C_{LD}	36.34	35.12	31.92	27.70	26.77	24.43

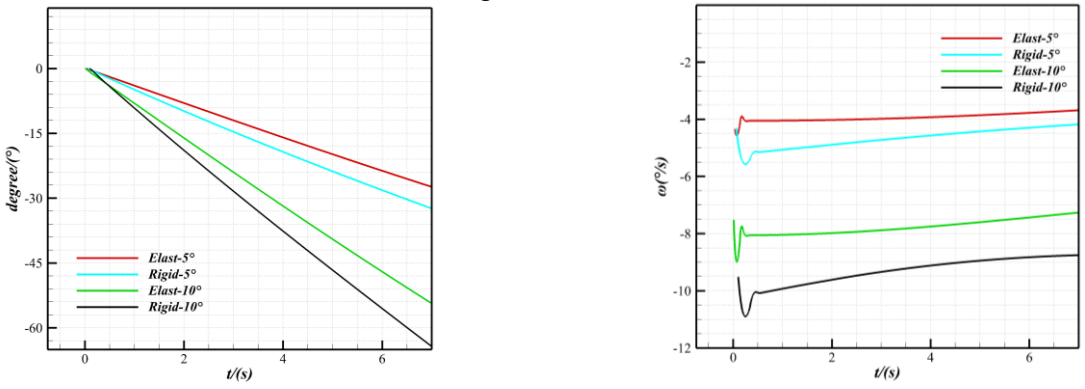
Table 9 Mach=0.85 Aerodynamic Parameters

	Rigid			Elastic		
Deflection	0°	5°	10°	0°	5°	10°
C_{mx}	0.1410E-4	0.6841E-2	0.1632E-1	0.2632E-4	0.2841E-2	0.4969E-2
C_L	0.5699E0	0.5634E0	0.5491E0	0.3514E0	0.3494E0	0.3474E0
C_{LD}	16.84	16.57	15.68	14.81	14.28	13.27

From the comparison between Figure 14, Figure 15 and Figure 17, Figure 18, the results reveal that the static aeroelastic deformation characteristics of the full-model CRM wing are similar to those of the semi-model, and the overall deformation trend of the wing keeps consistent after aileron deflection. According to the result in Table 8 and Table 9, the roll moment coefficient induced by differential aileron deflection drops significantly by aeroelastic deformation in two Mach numbers. The reduction reaches approach 46% at Ma 0.63, and becomes much larger at Ma 0.85. In addition, the decrease of lift coefficient further causes the decline of lift-drag ratio, which cannot be revealed by simulation of CRM semi-model wing.

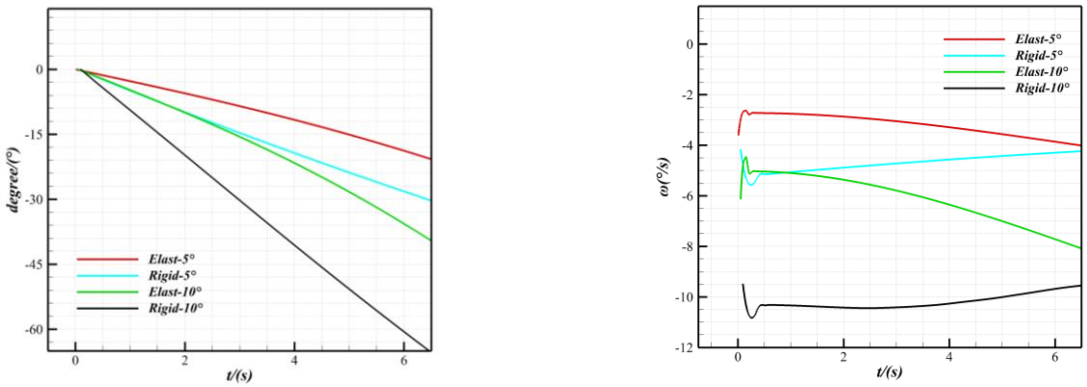
4.2 Dynamic Roll Maneuverability Calculation with Aeroelasticity

With the roll degree of freedom released for computation, the resulting roll angle and roll rate responses are presented by Figure 19 and Figure 20.



(a) Roll Angle (b) Roll Rate

Figure 19 Mach=0.63



(a) Roll Angle (b) Roll Rate

Figure 20 Mach=0.85

During the Figure 19 and Figure 20, *Elast* denotes the roll response calculation of the aeroelastic-coupled wing, while *Rigid* refers to the analysis of the rigid wing; 5° and 10° correspond to the differential aileron deflection angles.

The results in Figure 19 and Figure 20 show that aeroelastic effects significantly degrade the wing's dynamic rolling maneuverability under both Mach 0.63 and Mach 0.85 conditions, which is consistent with the static aileron effectiveness results presented in Tables 8 and 9.Through comparison of roll response results under the two Mach number conditions, reveals that at Ma = 0.63, the roll rate variations of the elastic and rigid wings follow similar trends. However, at Ma = 0.85, the roll rate trends of the two configurations are opposite at the initial instant of aileron deflection; And They also exhibit distinct variation trends over time, the roll rate of the elastic wing increases with time, while that of the rigid wing gradually decreases.

5. Conclusion

To explore the influence of aeroelastic deformation on aileron efficiency of high-aspect-ratio flexible wings, an enhanced modal approach is developed to capture geometric nonlinearity under the large flexible deformation while maintaining the simplicity of modal approach in solving structural deformation. Combined with CFD, researches on static aileron efficiency and dynamic roll maneuverability characteristics are conducted based on the CFD/CSD coupled framework. The main conclusions are summarized as follows:

1. Static aeroelastic deformation causes redistribution of aerodynamic loads on CRM wings. Influenced by the geometric twist and swept configuration of the CRM wing, strong bending-torsion coupled deformation emerges during aeroelastic computation, leading to a reduction in aerodynamic lift. Reverse bending phenomenon appears near the wing tip under transonic flow conditions, but it does not occur in subsonic flow.

2. Aeroelastic deformation cause the reduction of static aileron efficiency. Greater structural deformation occurs at the wing tip area, hence the efficiency of outboard ailerons experiences more severe decrease under aeroelastic effects. As transonic conditions are closer to the critical speed of aileron reversal, the efficiency decline of outboard ailerons is more remarkable than that under subsonic conditions.

3. Aeroelastic analysis on full-model wings indicates that aeroelastic deformation reduces the static efficiency of differentially deflected ailerons and weakens dynamic rolling maneuver performance. The degradation of rolling capability is much more significant in transonic flow. Under subsonic conditions, the roll rate of both rigid and elastic wings declines gradually with time. But for transonic conditions, rigid wings follow the same rule, while the roll rate of elastic wings increases with time spending.

6. Contact Author Email Address

Yue Zhao: zhaoyue706@qq.com

7. Copyright Statement

The authors confirm that they, and/or their company or organization, hold copyright on all of the original material included in this paper. The authors also confirm that they have obtained permission,

from the copyright holder of any third party material included in this paper, to publish it as part of their paper. The authors confirm that they give permission, or have obtained permission from the copyright holder of this paper, for the publication and distribution of this paper as part of the ICAS proceedings or as individual off-prints from the proceedings.

References

[1] M. Castellani, J. E. Cooper, and Y. Lemmens, "Nonlinear static aeroelasticity of high-aspect-ratio-wing aircraft by finite element and multibody methods," Journal of Aircraft, vol. 54, no. 2, pp. 1–13, 2016.

[2] Ma Y, Elham A. Designing high aspect ratio wings: A review of concepts and approaches. Progress in Aerospace, 2024, Vol. 145.

[3] C. E. S. Cesnik, R. Palacios, and E. Y. Reichenbach, "Reexamined structural design procedures for very flexible aircraft," Journal of Aircraft, vol. 51, no. 5, pp. 1580–1591, 2014.

[4] D. W. Chen and G. W. Yang, "Research on static aeroelastic calculation methods," Acta Mechanica Sinica, vol. 41, no. 4, pp. 469–479, 2009.

[5] Ritter M, Jones J and Cesnik CES. Enhanced modal approach for free-flight nonlinear aeroelastic simulation of very flexible aircraft. Proc 15th Dynamics Specialists Conference, pp. 2016-1794, 2016.

[6] Y. Z. Yang, H. Zhang, Y. S. Gu, and M. Song, "Aeroelastic analysis of high-aspect-ratio wings considering geometric nonlinear effects," Journal of Vibration and Shock, vol. 33, no. 16, pp. 72–75, 2014.

[7] He X, Wang X and Tang G. Wind Tunnel Testing of Flexible Wing Model with Aileron Freeplay Nonlinearity. AIAA Aviation Forum and Exposition, paper 2021-2534, 2021.

[8] Stanford, Bret K.Optimal Control Surface Layout for an Aeroservoelastic Wingbox[J]. AIAA Journal, vol.55, no.12, pp.4347-4356, 2017.

[9] Ritter M, Cesnik CES and Krüger WR. An enhanced modal approach for large deformation modeling of wing-like structures. 56th AIAA/ASCE/AHS/ASC Structures, Structural Dynamics, and Materials Conference, pp 332-347, 2015.

[10] Meirovitch L, "Hybrid state equations of motion for flexible bodies in terms of quasi-coordinates," Journal of Guidance, Control, and Dynamics, vol. 14, no. 5, pp. 1008–1013, 1991.

[11] Waszak M, John BE and Schmidt DK. A simulation study of the flight dynamics of elastic aircraft. Proc AIAA Atmospheric Flight Mechanics Conference, Monterey, CA, USA, 1987

[12] Hallissy B and Cesnik C. High-fidelity Aeroelastic Analysis of Very Flexible Aircraft. Proc 52nd AIAA/ASME/ASCE/AHS/ASC Structures, Structural Dynamics and Materials Conference, 2012.

[13] Smith MJ, Patil MJ and Hodges DH. CFD-based analysis of nonlinear aeroelastic behavior of high-aspect ratio wings. Proc 19th AIAA Applied Aerodynamics Conference, 2001..